UNIVERSITY OF AMSTERDAM

UvA-DARE (Digital Academic Repository)

Quantitative and localized spectroscopy for non-invasive bilirubinometry in neonates

Bosschaart, N.

Publication date
2012

Link to publication

Citation for published version (APA):
Bosschaart, N. (2012). *Quantitative and localized spectroscopy for non-invasive bilirubinometry in neonates*. [Thesis, fully internal, Universiteit van Amsterdam].

General rights
It is not permitted to download or to forward/distribute the text or part of it without the consent of the author(s) and/or copyright holder(s), other than for strictly personal, individual use, unless the work is under an open content license (like Creative Commons).

Disclaimer/Complaints regulations
If you believe that digital publication of certain material infringes any of your rights or (privacy) interests, please let the Library know, stating your reasons. In case of a legitimate complaint, the Library will make the material inaccessible and/or remove it from the website. Please Ask the Library: https://uba.uva.nl/en/contact, or a letter to: Library of the University of Amsterdam, Secretariat, Singel 425, 1012 WP Amsterdam, The Netherlands. You will be contacted as soon as possible.

UvA-DARE is a service provided by the library of the University of Amsterdam (https://dare.uva.nl)

Download date:08 Feb 2025

CHAPTER 3

Optical properties of neonatal skin measured *in vivo* as a function of age and skin pigmentation

Knowledge of the optical properties of neonatal skin is invaluable when developing new, or improving existing optical techniques for use at the neonatal intensive care. In this Chapter, we present *in vivo* measurements of the absorption μ_a and reduced scattering coefficient μ_s' of neonatal skin between 450 and 600 nm and assess the influence of age and skin pigmentation on the optical properties.

The optical properties were measured using a spatially resolved, steady state diffuse reflectance spectroscopy setup, combined with a modified spatially resolved diffusion model. The method was validated on phantoms with known values for the absorption and reduced scattering coefficient. Values of μ_a and μ_s' were obtained from the skin at four different body locations (forehead, sternum, hand and foot) of 60 neonates with varying gestational age, postnatal age and skin pigmentation.

We found that μ_a ranged from 0.02-1.25 mm^{-1} and μ_s' was in the range of 1-2.8 mm^{-1} (5^{th} – 95^{th} percentile of the patient population), independent of body location. In contrast to previous studies, no to very weak correlation was observed between the optical properties and gestational maturity, but a strong dependency of the absorption coefficient on postnatal age was found for dark skinned patients.

This work has been published in: N. Bosschaart, R. Mentink, J.H. Kok, T.G. van Leeuwen, M.C.G. Aalders, "Optical properties of neonatal skin measured *in vivo* as a function of age and skin pigmentation", *Journal of Biomedical Optics* 16(9), 097003 (2011)

3.1 Introduction

Light-tissue interactions in the visible wavelength range are the basis of many experimental and routinely used diagnostic and therapeutic procedures at the neonatal intensive care – e.g. in transcutaneous bilirubinometry [1], pulse oximetry [2] and phototherapy during jaundice [3]. Knowledge of the optical properties of the tissue is essential when predicting or modeling light-tissue interactions, which in turn is invaluable for the development and improvement of these procedures. Although the majority of optical techniques at the neonatal intensive care depend on the interaction of light with skin, very little information can be found in literature about the optical properties (e.g. absorption and scattering coefficients) of neonatal skin.

Earlier research on the optical properties of neonatal skin was performed by Saidi *et al*, who measured the absorption coefficient and the reduced scattering coefficient as a function of age with an integrating sphere setup [4,5]. They found that the reduced scattering coefficient increases with age, due to maturation of the skin. These measurements were performed *in vitro* on excised non-pigmented skin. However, optical properties measured *in vitro* may differ substantially from those measured *in vivo* due to the unavoidable sample preparation procedures [6]. Moreover, it is expected that the absorption coefficient depends on skin pigmentation, which was not investigated. We expect that optical properties of neonatal skin, assessed by *in vivo* measurements as a function of age and skin pigmentation, can assist many optical devices such as transcutaneous bilirubinometers in improving their performance. The readings of current bilirubinometers commonly have a spread of ±40 μmol/L around the bilirubin concentration (ranging from 0 – 400 μmol/L) that is measured by the gold standard for bilirubin measurements, total serum bilirubin analysis [1]. This inaccuracy may be partly caused by variations in the often unknown probed volume inside the skin. Knowledge of the optical properties can be used as input to, for example, Monte Carlo simulations of photon distributions inside the skin. These simulations can provide insight into the probed tissue volume, which in turn can lead to a more optimal design for optical diagnostic probes, methods of analysis and comparison between devices.

Steady state, spatially resolved diffuse reflectance spectroscopy has proven to be a reliable technique for measuring the optical properties of tissue and tissue simulating phantoms in the near infrared [7,8] and visible [8,9] wavelength range. When using short source-detector distances, the investigated tissue volume is small [9] and can be confined to, for instance, the skin. Therefore, in this study we used a steady state, spatially resolved diffuse reflectance spectroscopy setup and a semi-empirical 3D-diffusion model, modified for our detection geometry, to measure the absorption and reduced scattering coefficient of neonatal skin from 450 – 600 nm.

The optical properties were measured on the skin of 60 preterm neonates with varying gestational maturity, postnatal age and skin pigmentation. All measurements were performed on four body locations (forehead, sternum, hand and foot), which are common measurement sites for either transcutaneous bilirubinometry, or pulse oximetry. The method was validated on phantoms with known values for the absorption and reduced scattering coefficient.

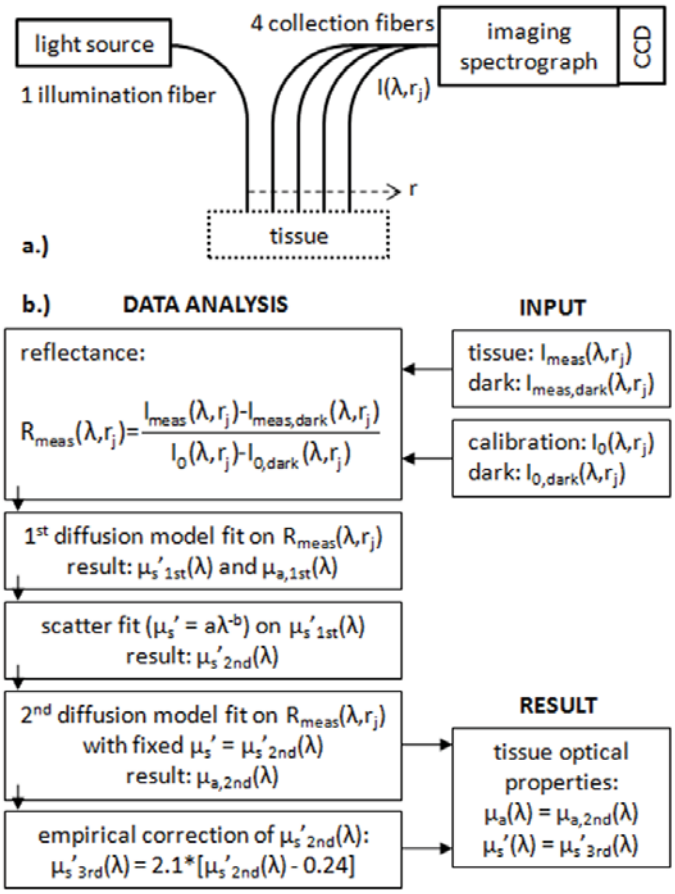

Figure 3.1 *a) Illustration of the measurement setup. b) Schematic illustration of the data analysis.*

3.2 Methods

3.2.1 Experimental setup

The diffuse reflectance spectroscopy setup (similar to that of Doornbos *et al* [7] and Nichols *et al* [8]) is shown in Figure 3.1a. Tissue illumination and detection of re-emitted light are performed by a multi-fiber probe. The probe consists of 5 fibers (400 µm core diameter, length ~2 m) which are cast in-line in an aluminum sensing head with a core-to-core distance of 600 µm. The first fiber acts as the illumination fiber and guides the white light from a tungsten halogen source (AvaLight-HAL, Avantes, USA) to the tissue. The other four fibers detect the re-emitted light (source-detector distances of r_1 = 0.6 mm, r_2 = 1.2 mm, r_3 = 1.8 mm, r_4 = 2.4 mm) and guide it to an imaging spectrograph (Olympus ISS, Olympus, USA). A 16-bit 128 x 1024 pixel CCD camera (DH501-18F-01, Andor Technology, USA) cooled to 0 ^{o}C detects the four spectra originating at different distances from the illumination fiber, with a wavelength resolution of 9 nm over the detection range of 400 to 820 nm. The image tracks illuminated by the fibers are averaged for each fiber to obtain four averaged spectra. The total exposure time for the

in vivo measurements ranged between 15 and 35 ms. In order to minimize system noise and to correct for temporal variation, each measurement in this Chapter consists of the average of three subsequent measurements with an interval of 1s.

3.2.2 Setup calibration

The diffuse reflectance measurements require three types of calibration: 1) wavelength calibration of the spectrograph, 2) calibration to correct for the collection efficiency of the setup and the spectral emission of the source and 3) correction for the (small amount of) ambient light and system noise.

The wavelength calibration of the spectrograph is performed by measuring the emission of a 543 nm and a 633 nm HeNe laser, and the emission of a fluorescent lamp. An additional calibration is done prior to each patient/phantom measurement by measuring the spectrum of a fluorescent light tube. The collection efficiency of the setup and the spectral emission of the source are calibrated using the method described in detail by Doornbos *et al* [7], which comprises measuring the collected intensity for each detection fiber at the entrance of an integrating sphere, illuminated by the illumination fiber of the probe. This calibration results in a calibration spectrum for each fiber distance r_j, indicated by $\mathbf{I_0}(r_j)$ (all wavelength dependent parameters in this Chapter will be denoted by a bold-faced character).

To correct for the collection of ambient light and system noise, a dark measurement was taken prior to each patient/phantom measurement with a shielded probe. The dark measurement results in a dark spectrum for each fiber distance, indicated by $\mathbf{I_{dark}}(r_j)$.

3.2.3 Data analysis

To extract the absorption and reduced scattering coefficient from the acquired spectra, we use the steady state diffusion approximation to the photon transport equation described by Farrell *et al* [10]. This diffusion model describes the 3D photon distribution inside a medium for photons injected by a point source, by modeling an isotropic source at a depth $\mathbf{z_0}$ inside the tissue and a virtual source at a distance of $2\mathbf{z_b}+\mathbf{z_0}$ above the medium. The remittance $\mathbf{R_{theor}}$ at the tissue surface as a function of source-detector distance r, and the optical properties of the tissue is given by [10]:

$$\mathbf{R_{theor}}(r) = \frac{1}{(4\pi)}\left[\frac{\mathbf{z_0}}{\mathbf{r_1^2}}\left(\boldsymbol{\mu}_{\mathbf{eff}} + \frac{1}{\mathbf{r_1}}\right)e^{-\boldsymbol{\mu}_{\mathbf{eff}}\cdot\mathbf{r_1}} + \frac{(\mathbf{z_0}+2\mathbf{z_b})}{\mathbf{r_2^2}}\left(\boldsymbol{\mu}_{\mathbf{eff}} + \frac{1}{\mathbf{r_2}}\right)e^{-\boldsymbol{\mu}_{\mathbf{eff}}\cdot\mathbf{r_2}}\right] \tag{3.1}$$

where $\boldsymbol{\mu}_{\mathbf{eff}} = [3\boldsymbol{\mu}_a(\boldsymbol{\mu}_a + \boldsymbol{\mu}_s')]^{½}$, $\mathbf{r_1} = (\mathbf{z_0}^2 + r^2)^{½}$, $\mathbf{r_2} = [(\mathbf{z_0} + 2\mathbf{z_b})^2 + r^2]^{½}$, $\mathbf{z_0} = (\boldsymbol{\mu}_a + \boldsymbol{\mu}_s')^{-1}$, and $\mathbf{z_b} = 2/3\cdot A(\boldsymbol{\mu}_a + \boldsymbol{\mu}_s')^{-1}$. Note that all parameters, except r, are wavelength dependent. The value of the empirical parameter A in the definition of $\mathbf{z_b}$ was set to A=1, since this gave the most reliable results (i.e. smallest residuals) when fitting our model to the data. Fitting the diffusion model to the spatially measured reflectance of the four detection fibers all together, using $\mathbf{R_{meas}}(r_j) = \alpha\cdot\mathbf{R_{theor}}(r_j)$ yields a single set of the parameters $\boldsymbol{\mu}_a$ and $\boldsymbol{\mu}_s'$. The proportionality factor α is adapted from Doornbos *et al* [7] and contains factors like the numerical aperture and the efficiency of coupling light into the sample. The value of α was found by fitting the diffusion model to the reflectance of a phantoms with known $\boldsymbol{\mu}_a$ and $\boldsymbol{\mu}_s'$ (Section 3.2.4).

Our method of analysis (schematically depicted in Figure 3.1b) can be explained in the following steps, in which we adapted steps 1 to 4 from Doornbos *et al*: 1) calculation of the measured reflectance for each fiber distance: $\mathbf{R_{meas}}(r_j) = [\mathbf{I_{meas}}(r_j) - \mathbf{I_{meas,dark}}(r_j)]/[\mathbf{I_0}(r_j) - \mathbf{I_{0,dark}}(r_j)]$, 2) fitting the diffusion model to $\mathbf{R_{meas}}(r_j)$, using a nonlinear least-square Levenberg-Marquardt algorithm, which results in a first approximation for the wavelength dependent absorption and reduced scattering coefficient $\boldsymbol{\mu_{a,1st}}$ and $\boldsymbol{\mu_s'_{1st}}$, 3) fitting the function $\boldsymbol{\mu_s'} = a\lambda^{-b}$ (where b is the scatter power and both a and b are free running fit parameters) to the obtained $\boldsymbol{\mu_s'_{1st}}$ using a nonlinear least-square Levenberg-Marquardt algorithm, which results in a second approximation for the reduced scattering coefficient $\boldsymbol{\mu_s'_{2nd}}$, 4) re-fitting the diffusion model to $\mathbf{R_{meas}}(r_j)$ with $\boldsymbol{\mu_s'_{2nd}}$ as a fixed parameter, which results in a second approximation for the absorption coefficient $\boldsymbol{\mu_{a,2nd}}$, 5) correction of $\boldsymbol{\mu_s'_{2nd}}$ for an initial underestimation using the empirically determined relation $\boldsymbol{\mu_s'_{3rd}} = 2.1*(\boldsymbol{\mu_s'_{2nd}} - 0.24)$ (see Section 3.3.1). The obtained values for $\boldsymbol{\mu_{a,2nd}}$ and $\boldsymbol{\mu_s'_{3rd}}$ are regarded as the bulk optical properties of the tissue in the measurement volume, from now on indicated by $\boldsymbol{\mu_a}$ and $\boldsymbol{\mu_s'}$.

The diffusion model is valid for semi-infinite, homogeneous media where scattering dominates absorption ($\boldsymbol{\mu_a}/\boldsymbol{\mu_s'} \leq \beta$, commonly with $\beta << 1$) and a source-detector separation that ensures a diffuse photon distribution ($r > \gamma/(\boldsymbol{\mu_a}+\boldsymbol{\mu_s'})$, commonly r is at least one mean free path, $1/(\boldsymbol{\mu_a}+\boldsymbol{\mu_s'})$, hence $\gamma=1$). Note that for our probe geometry, the value of γ depends entirely on the lowest value of $(\boldsymbol{\mu_a}+\boldsymbol{\mu_s'})$ that can be accurately measured, since the (minimal) source-detector separation r is fixed. To determine the validity and accuracy of the model for our measurement geometry and neonatal skin, we performed measurements on phantoms with optical properties in the range of neonatal skin and found the limiting values for β and γ (Section 3.3.1). In contrast to Doornbos *et al*, who could only reliably measure the optical coefficients for wavelengths larger than 600 nm, we found that $r > \gamma/(\boldsymbol{\mu_a}+\boldsymbol{\mu_s'})$ is in general only valid for wavelengths shorter than 600 nm. This can be explained by a difference in probe design (i.e. shorter source-detector separations) and the relatively low value of $\boldsymbol{\mu_s'}$ for neonatal skin. Therefore, we only determined the optical properties in the 450-600 nm wavelength region of the signal. The homogeneity of neonatal skin was investigated by optical coherence tomography (OCT) measurements (Section 3.4.3).

3.2.4 Phantom validation study

The method of analysis described above was validated with measurements on 14 phantoms with known values for $\boldsymbol{\mu_a}$ and $\boldsymbol{\mu_s'}$. The optical properties of the phantoms ($\boldsymbol{\mu_a}$= 0–2.7 mm^{-1}, $\boldsymbol{\mu_s'}$= 0.3–3.7 mm^{-1}) were chosen to be in the same range as the expected values of $\boldsymbol{\mu_a}$ and $\boldsymbol{\mu_s'}$ of neonatal skin. The phantoms consisted of two series: series 1, with a fixed concentration of 1.5% Intralipid (Intralipid®20%, Fresenius Kabi, Germany) and varying concentrations of a non-scattering, absorbing magenta dye (0.125-2%, Ecoline #337, Royal Talens, The Netherlands), and series 2, with a fixed concentration of 0.25% magenta dye and varying concentrations of Intralipid (0.25-2%). The reduced scattering coefficient of the phantoms was estimated using the predictions of Van Staveren *et al* [11] for $\boldsymbol{\mu_s'}$ of Intralipid. The absorption coefficient of the dye only was determined in a separate transmission measurement by a spectrograph (USB4000, Ocean Optics, USA). During the measurements, the probe was in contact with the phantoms to minimize reflections from the phantom surface. From these phantom

measurements, we determined the accuracy of our determination of μ_a and μ_s' and the validity limits of our analysis, i.e. the limiting values of β and γ (i.e. $\mu_a/\mu_s' \leq \beta$ and $r > \gamma/(\mu_a+\mu_s')$) for which the diffusion model can be applied in this measurement geometry.

To verify that comparison with the predicted μ_s' of Van Staveren is justified for these phantoms, we also measured the μ_s' of National Institute of Standards and Technology (NIST)-certified spheres with a diameter of 409 nm, suspended in water (0.48 volume%, μ_s' = 2-3 mm^{-1}, Thermo Scientific USA). The measured μ_s' of this phantom was compared to the theoretical μ_s', obtained from Mie theory.

For measurements of the optical properties of neonatal skin, it is important that the measurement volume is confined to the skin only. Therefore, knowledge of the probing depth is required. To investigate the probing depth of the system, the probe was submersed at varying distances (0–5 mm, in steps of 100 μm) from the lower bottom of a phantom with μ_a and μ_s' similar to neonatal skin (1.5% Intralipid, 0.5% dye: μ_a up to 0.35 mm^{-1}, μ_s' = 2 – 2.6 mm^{-1}). The lower bottom of the liquid phantom consisted of a stationary solid layer of diffusively scattering white rubber. The measurements were repeated with a diffusively scattering black rubber layer at the lower bottom.

3.5.5 Patient study

60 Neonates of the neonatal intensive care unit in the Academic Medical Center of Amsterdam were enrolled in this study. Approval of the medical ethical committee and informed consent from the patient's legally authorized representative were obtained. The patient group varied in gestational age (i.e. pregnancy duration): 29.4 ± 3.3 weeks (mean ± sd, normal distribution), postnatal age: 11 (6-28) days (median (25^{th} – 75^{th} percentile), non-normal distribution) and skin type. The skin type of the patients was classified into three categories, based on observation and ethnicity of the patient and the parents: type 1 (Caucasian or 'white': 43 patients), type 2 (Mediterranean or 'intermediate': 12 patients) and type 3 (Negroid or 'dark': 5 patients). The majority of the patients were subjected to more than one measurement during their admission at the hospital, with a time lapse of one day to several weeks between measurements and a median of 3 measurements per patient. An overview of the patient population and the number of measurements is listed in Table 3.1A.

The optical properties were determined at four locations on the skin: the glabella of the forehead, the lower end of the sternum, the plantar side of the foot and the dorsal side of the hand. The presence of visible large blood vessels in the measured volume was avoided. Due to medical reasons (e.g. presence of a ventilator, pulse oximeter and/or intravenous line), not all skin areas were accessible at all times, resulting in a different number of measurements between locations (Table 3.1A). To minimize reflections from the probe-tissue interface, the probe surface was covered with lubricating gel (Euroband Pedicat, Pollak, France). Attention was paid to keep a constant probe pressure on the skin during the measurements.

A general linear multivariate analysis model in SPSS for Windows (version 16.0, SPSS Inc.) was used to assess the influence of measurement location and skin type on the optical coefficients at three wavelengths (475, 525 and 575 nm), where we assumed a normal distribution of the data. To avoid the influence of dependent measurements in the multivariate analysis, one measurement event per patient (including all four locations) was randomly selected from our dataset.

To investigate the anatomy and homogeneity of neonatal skin compared to adult skin, Optical Coherence Tomography (OCT) B-scans were made with a 1310 nm OCT system (HSL-2000, Santec, Japan) at the four investigated skin areas of several patients and adults.

Table 3.1 *Overview of the patient population and number of measurements per skin type and measurement location*

	A. all measurements				**B. measurements within validity limits**			
	type 1	type 2	type 3	all	type 1	type 2	type 3	all
Location	# measurements				# measurements			
forehead	137	47	33	217	132	45	10	187
sternum	135	41	29	205	133	39	9	181
hand	137	47	30	214	134	41	11	186
foot	136	49	33	218	136	48	32	216
	# patients				# patients			
forehead	43	12	5	60	42	12	4	58
sternum	43	12	5	60	43	12	4	59
hand	42	12	5	59	42	12	5	59
foot	42	12	5	59	42	12	5	59
total # patients	43	12	5	60	43	12	5	60
gestational age (wks) mean (± sd)	29.9 (±3.7)	29.2 (±1.8)	27.4 (±2.3)	29.4 (±3.3)	29.9 (±3.7)	29.2 (±1.8)	27.5 (±2.3)	29.4 (±3.3)
postnatal age (days) median (p25-p75)	11 (6-35)	6 (4-13)	18 (9-34)	11 (6-28)	11 (6-35)	6 (4-13)	18 (10-32)	11 (6-28)

3.3 Results - phantom validation study

3.3.1 Validity and accuracy

Figure 3.2a and 3.2b show the measured $\boldsymbol{\mu_s'_{2nd}}$ and $\boldsymbol{\mu_a}$ versus the expected values (from Van Staveren and transmission spectroscopy, respectively) for all phantoms of series 1 and 2. Difference is made between phantoms for which the validity limits (i.e. $\boldsymbol{\mu_a/\mu_s'} \leq \beta$ and $r > \gamma/(\boldsymbol{\mu_a}+\boldsymbol{\mu_s'})$) are valid for all wavelengths (black lines) and phantoms for which the validity limits are not valid for at least one wavelength between 450-600 nm (red lines). The obtained values for β and γ will be described below.

From Figure 3.2b, we can conclude that $\boldsymbol{\mu_a}$ is predicted with 15% accuracy by our measurements up to a value of 1.7 mm^{-1}. Since the corresponding expected μ_s' = 2.3 mm^{-1} for this value of μ_a, we conclude that the limiting ratio between $\boldsymbol{\mu_a}$ and $\boldsymbol{\mu_s'}$ for which the diffusion model can be applied in this measurement geometry, is β = ¾. This

value of β is considerably higher than the commonly used value β = 1/10 in other diffusion model based studies [7,8]. For the phantoms where $\mu_a/\mu_s' \leq ¾$ is not valid, μ_a is underestimated by our measurement.

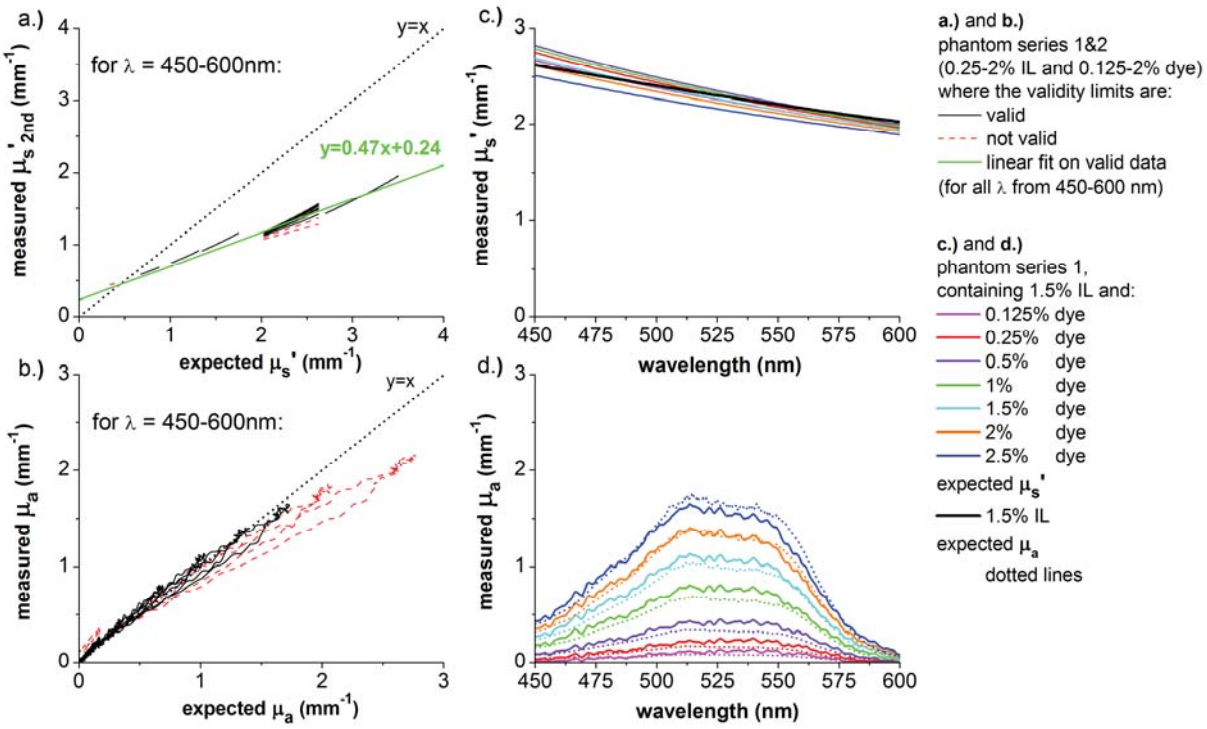

Figure 3.2 *Phantom validation study. For all phantoms in series 1&2: a.) measured $\mu_s'_{2nd}$ vs. expected μ_s', and b.) measured μ_a vs. expected μ_a. Difference is made between phantoms for which $\mu_a/\mu_s' \leq 6$ and $r > \gamma/(\mu_a+\mu_s')$ are valid (black lines) and not valid (red lines). For all phantoms in series 1 for which $\mu_a/\mu_s' \leq 6$ is valid: c.) measured μ_s' after correction and expected value vs. wavelength and d.) measured and expected μ_a vs. wavelength.*

Figure 3.2a shows a consistent underestimation of $\mu_s'_{2nd}$, which can be described by the linear relation ($\mu_s'_{2nd} = 0.47\mu_s'_{expected} + 0.24$) for the range of μ_s'-values within the validity limits. Exactly the same linear relation was found between the measured $\mu_s'_{2nd}$ of the 409 nm NIST certified spheres and the expected μ_s' from Mie theory (no graph), indicating that the underestimation is consistent and not caused by incorrect comparison to the prediction of Van Staveren. We therefore corrected all measured $\mu_s'_{2nd}$ (phantom and tissue measurements) for this underestimation, using the linear relation $\mu_s' = \mu_s'_{3rd} = 2.1*(\mu_s'_{2nd} - 0.24)$.

Figure 3.2c and 3.2d show the measured μ_s' after correction and the measured μ_a versus wavelength for the phantoms of series 1 for which the validity limits are valid. Since the Intralipid concentration is fixed for the phantoms of series 1, μ_s' is expected to be equal for all phantoms. After correction, the measured μ_s' agree within 10% with the prediction of Van Staveren and a maximum variation of 10% can be observed between the measured μ_s' of all phantoms. As expected from Figure 3.2b, the measured μ_a in

Figure 3.2d agree within the reported accuracy with the expected μ_a from transmission spectroscopy.

We obtained the value of γ from the phantom series 2 with fixed μ_a and varying μ_s'. For these series, the μ_a and μ_s' were predicted correctly for the phantoms with $(\mu_a+\mu_s')> 0.8$ mm^{-1}. For the phantom with $(\mu_a+\mu_s')< 0.8$ mm^{-1}, μ_a was overestimated by our measurement. Since the minimal source-detector separation is 0.6 mm in our measurement geometry, we conclude that γ = ½ in the validity limit $r > \gamma/(\mu_a+\mu_s')$.

Summarizing, our method is valid when measuring on semi-infinite homogeneous media with values of μ_a and μ_s' that meet the validity limits $\mu_a/\mu_s' \leq ¾$ and $(\mu_a+\mu_s')> 0.8$ mm^{-1}. Our phantom study shows that these limits hold for this specific probe geometry and method of analysis. When measuring on neonatal skin, the validity of these limits needs to be investigated for every wavelength within the measured spectral range. Since we need to apply the empirically determined correction on the initial value of $\mu_s'_{2nd}$, our method of analysis based on the diffusion model is semi-empirical.

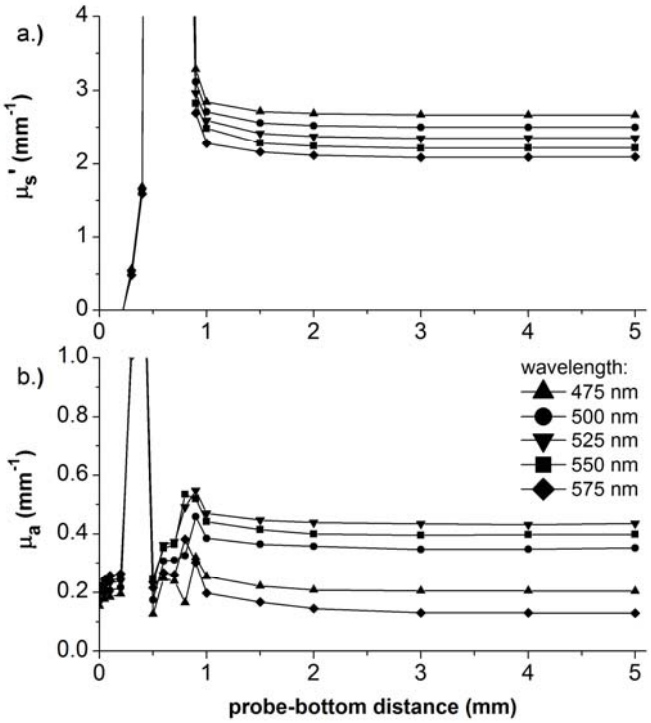

Figure 3.3 *Measured values of a.) μ_s' and b.) μ_a as a function of probe-bottom distance for the 1.5%Intralipid-0.5%dye phantom and the black bottom layer. Results are shown for the wavelengths 475, 500, 525, 550 and 575 nm.*

3.3.2 Probing depth

Figure 3.3 a and b show the dependency of the measured coefficients on the probe-bottom distance for the phantom with the black bottom layer. For probe-bottom distances < 1 mm, the measured coefficients are inconsistent, due to presence of the black bottom layer in the measurement volume. For probe-bottom distances ≥ 1 mm, the measured μ_a and μ_s' are consistent and agree with the expected values within the reported accuracy. Also for the phantom with the white bottom layer, the measured μ_a and μ_s' are consistent for distances ≥ 1 mm. We therefore conclude that the probing

depth of the system is 1 mm for homogeneous media with optical properties comparable to the 1.5%Intralipid-0.5%dye phantom (i.e. μ_s' ≈ 2.3 mm^{-1} and μ_a ≈ 0.4 mm^{-1}).

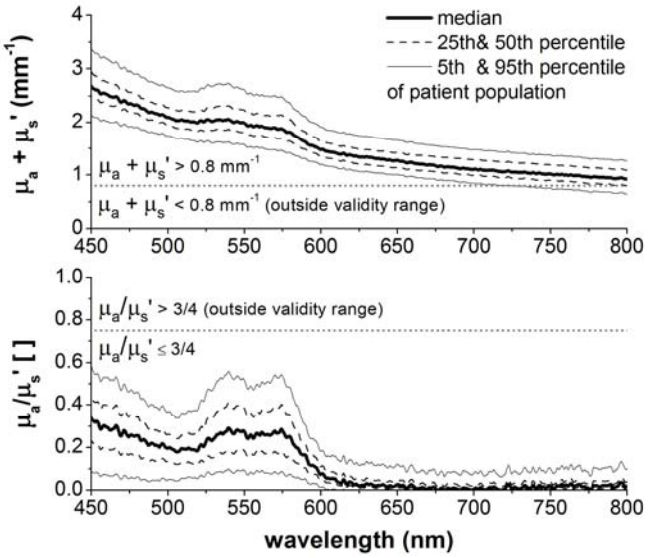

Figure 3.4 *Median values and 5th, 25th, 75th and 95th percentiles for the measured μ_a/μ_s' and ($\mu_a+\mu_s'$) vs. wavelength for the patient measurements at the foot, after selection of the data between 450-600 nm by the validity limits (i.e. $\mu_a/\mu_s' \leq ¾$ and ($\mu_a+\mu_s'$)> 0.8 mm^{-1}, Table 3.1B).*

3.4 Results - patient study

3.4.1 Dependency on location and age

The validity of the diffusion model ($\mu_a/\mu_s' \leq ¾$ and ($\mu_a+\mu_s'$)> 0.8 mm^{-1}) was checked for all patient measurements in the wavelength range of 450-600 nm, resulting in a reduction of the number of measurements and patients (Table 3.1B). Figure 3.4 shows the 5th to 95th percentiles of the selected patient measurements from Table 3.1B in the wavelength range of 450-800 nm. The validity of the limit ($\mu_a+\mu_s'$)> 0.8 mm^{-1} is in general not valid for the longer wavelengths, hence our choice to only show the optical properties from 450 to 600 nm. Within the wavelength range of 450-600 nm, all patient measurements fall well within the validity limits of our analysis. The μ_s' and μ_a for all patients and measurements in Table 3.1B are shown in Figure 3.5 for each location, regardless of skin type. The optical coefficients from this patient population were not normally distributed for all wavelengths; therefore we present μ_s' and μ_a with the median, and 5th, 25^{th,} 75th and 95th percentile. The median value for the scatter power b in μ_s' was 0.82 (forehead), 0.87 (sternum), 1.06 (hand) and 1.34 (foot). The multivariate analysis proved no significant differences ($p > 0.05$) in the optical coefficients between locations for each patient.

The dependencies of μ_s' and μ_a at λ = 600 nm on gestational maturity (gestational + postnatal age) are shown for the sternum in Figure 3.6 for all patients and measurements in Table 3.1B, regardless of skin type. After random selection of one measurement event per patient, no to very little correlation can be observed between μ_s' and gestational maturity (Spearman $r^2 = 0.14$, $p < 0.05$) and μ_a and gestational

maturity (Spearman $r^2 = 0.12$, $p < 0.05$). The same holds for the correlation between μ_s' and gestational maturity at the other locations (Spearman r^2 of 0.22 (forehead), 0.11 (hand) and 0.29 (foot), $p < 0.05$) and the correlation between μ_a and gestational maturity (Spearman r^2 of 0.06 (forehead), 0.01 (hand) and 0.10 (foot), $p < 0.05$). Similar results were obtained at other wavelengths.

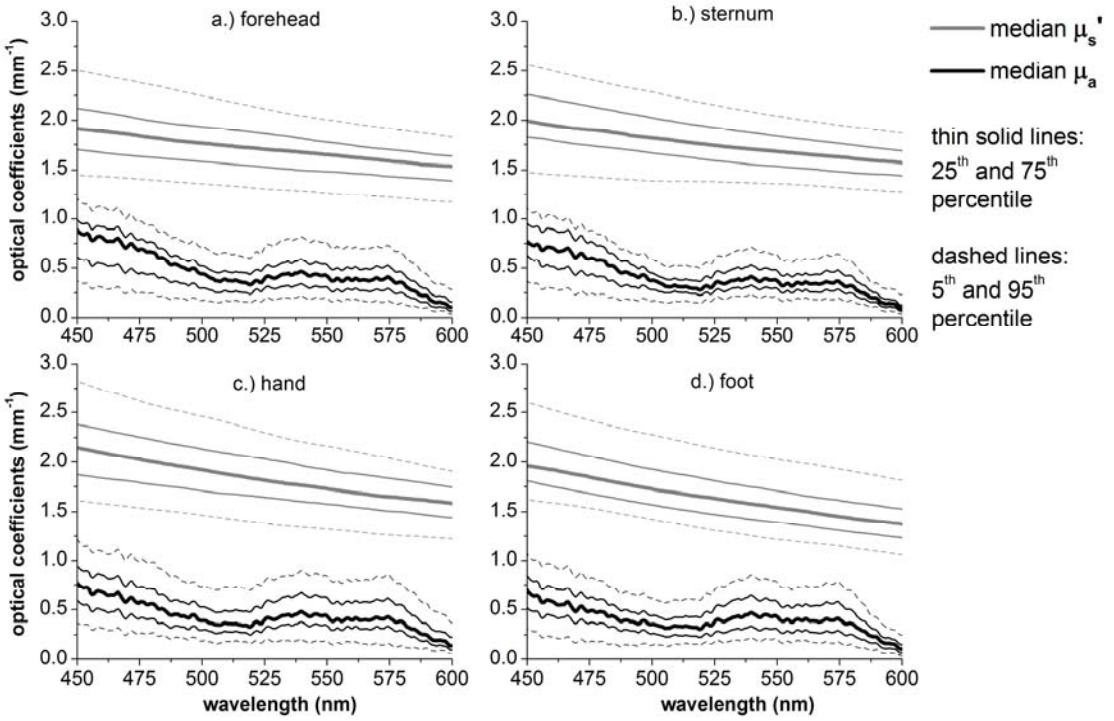

Figure 3.5 *For a.) forehead, b.) sternum, c.) hand and d.) foot: median values and 5th, 25th, 75th and 95th percentiles for the measured* μ_s' *and* μ_a *vs. wavelength for all patient measurements within the validity limits (Table 3.1B).*

3.4.2 Dependency on skin type

The median values of μ_a vs. wavelength are shown in Figure 3.7 for each skin type at the sternum (Figure 3.7a) and the foot (Figure 3.7b). Results for the forehead and the hand (no graph) were similar to those of the sternum. When only regarding the measurements that fall within the validity limits (solid lines, Table 3.1B), the multivariate analysis proved no significant ($p > 0.05$) influence of skin type on the measured optical properties, neither for μ_s' nor for μ_a. The latter is caused by exclusion of the highest μ_a values because of the the $\mu_a/\mu_s' \leq ¾$ validity limit, which is most abundant for patients with skin type 3 (Table 3.1). For the sternum, a larger difference in μ_a can be observed between the three skin types, if we analyze the median values of μ_a for all measurements in Table 3.1A (dotted lines, no elimination of measurements).

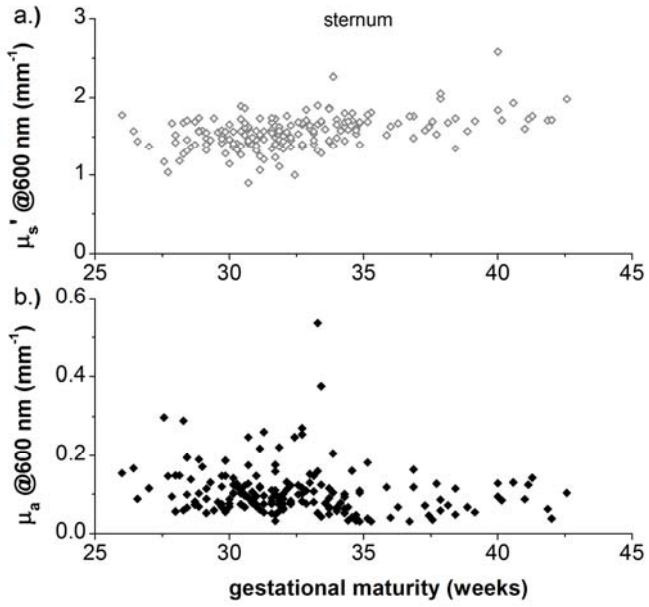

Figure 3.6 *Measured values at λ = 600 nm of a.) μ_s' and b.) μ_a, versus gestational maturity (gestational + postnatal age) at the sternum, for all patient measurements within the validity limits (Table 3.1B).*

This difference cannot be observed at the foot, which is likely to be due to the lack of melanin at this measurement site (plantar side of the foot). The results presented by the dotted lines in Figure 3.7 need to be interpreted with caution, because our model of analysis is not valid for these measurements. The presented values for μ_a are likely to be larger, considering the underestimation of μ_a for values beyond the $\mu_a/\mu_s' \leq ¾$ validity limit (Figure 3.2b). Hence, these results should be interpreted qualitatively (e.g. relative values, trends) rather than quantitatively.

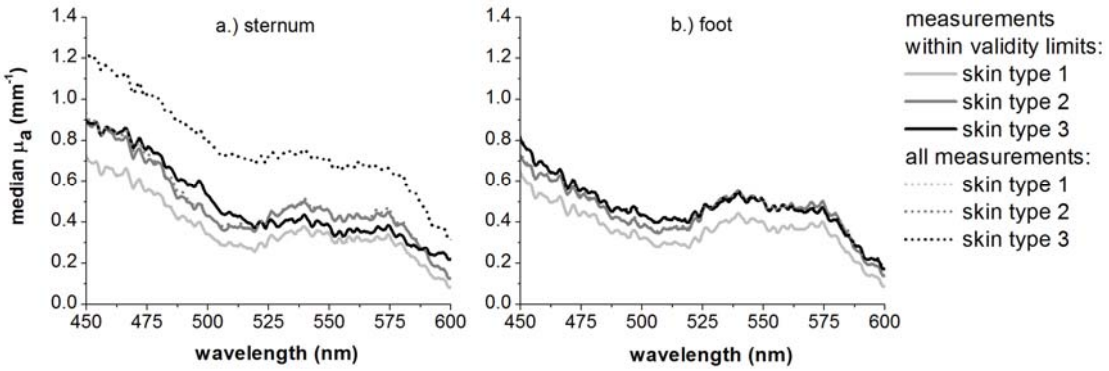

Figure 3.7 *Median values of μ_a vs. wavelength at a.) the sternum (upper graphs) and b.) the foot (lower graphs) for all measurements (dashed lines, Table 3.1A) and measurements within the validity limits (solid lines, Table 3.1B). Difference is made between skin types (type 1: Caucasian, type 2: Mediterranean, type 3: Negroid).*

The dependency of μ_a at λ = 600 nm on postnatal age is shown in Figure 3.8 at the sternum for each skin type. Also for these results, difference is made between the measurements where the validity limits are valid (closed symbols, Table 3.1B), and not valid (open symbols). A (qualitative) analysis of all measurements per skin type, yields a high correlation between the μ_a at 600 nm for skin type 3 and the postnatal age (Spearman $r^2 = 0.77$, $p < 0.05$). This can be ascribed to the stimulation of the production of melanin after birth [12]. The production of melanin for patients with skin type 2 and 1 is lower, resulting in less or no correlation with postnatal age (Spearman $r^2 = 0.18$ and 0.07, respectively, $p < 0.05$). Similar trends in μ_a vs. postnatal age were observed for the forehead and hand. The μ_a of the foot for patients with skin type 3 did not depend as much on age (Spearman $r^2 = 0.43$, $p < 0.05$) as for the other locations, due the lower melanin production at the measurement site (plantar side of the foot). Similar results were obtained at other wavelengths.

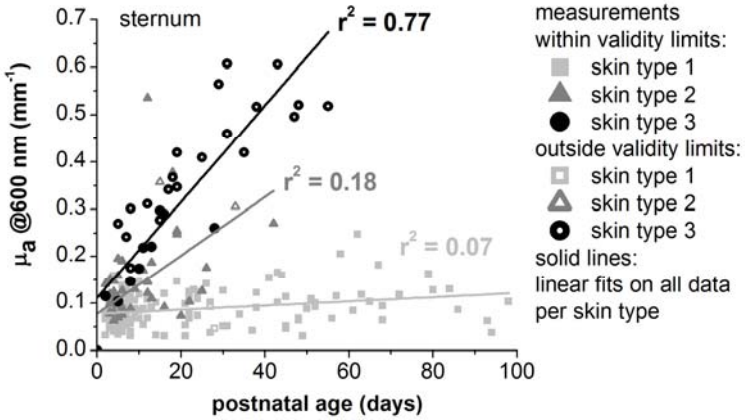

Figure 3.8 *Measured values for μ_a at λ = 600 nm vs. postnatal age at the sternum, for all patient measurements within the validity limits (filled symbols, Table 3.1B) and outside the validity limits (open symbols). Difference is made between skin types (type 1: Caucasian, type 2: Mediterranean, type 3: Negroid).*

3.4.3 OCT images of neonatal skin

Figure 3.9 a and b show typical OCT scans at 1310 nm of the skin at the foot of a patient (skin type 1, gestational age: 25 weeks, postnatal age: 56 days) and an adult (skin type 1, age: 25 years). No distinct layers can be observed in the skin of the neonate, which seems to extend beyond the imaging depth of approximately 1 mm. The skin of the adult shows more optical contrast between the individual skin layers and structures. Images at the sternum, forehead and hand gave similar results, as well as images for other patients and adults (results not shown).

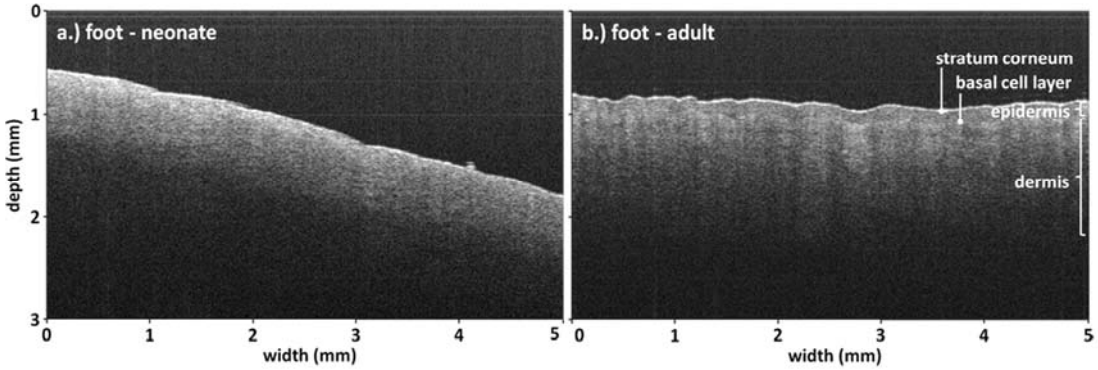

Figure 3.9 *OCT scans (1310nm) of the skin at the plantar side of the foot of a neonate (skin type 1, gestational age: 25 weeks, postnatal age: 56 days) and an adult (skin type 1, age: 25 years).*

3.5 Discussion

In this Chapter, we presented measurements of the optical properties of neonatal skin and assessed the influence of age and skin type on a large group of patients. This new knowledge on neonatal skin optical properties can aid to the development of optical techniques in neonatology. For instance, the measured values of μ_a and μ_s' can be used as input to Monte Carlo simulations of photon distributions inside the skin, which provide insight in e.g. optimal design for optical diagnostic probes.

3.5.1 Model validity - general

We used a spatially resolved, steady state diffuse reflectance spectroscopy setup and a steady state diffusion model to obtain the absorption and reduced scattering coefficient of the skin. Our method of analysis was validated in a phantom study (Section 3.3.1), by measuring μ_s' and μ_a of phantoms with known optical properties in the range of those of neonatal skin. We were able to measure μ_a with an accuracy of 15% and μ_s' with an accuracy of 10%, provided that the measurements were within the validity limits of the diffusion model ($\mu_a/\mu_s' \leq$ ¾ and $(\mu_a+\mu_s')> 0.8$ mm^{-1}). Other studies that analyze the spatially diffuse tissue reflectance with a diffusion model, typically allow more constrained validity limits [7,8], thereby eliminating more measurements. Reasons for this difference may be the choice for larger uncertainty margins in the limits of validity and other study design, such as measurement geometry and method of analysis. If, for instance, we do not apply the scatter power fit on the first outcome of the diffusion model fit to the measured reflectance and merely look at $\mu_{a,1st}$ and $\mu_{s,1st}'$ (Section 3.2.3), the value of β will be considerably lower.

This use of spectral constraints in diffusion model based analysis was investigated before by Kim *et al* [13] for source-detector separations similar to ours, and was thought to be the cause of extended validity limits, comparable to the limits found in this study. Measuring optical properties at small source-detector separations (< 1 mm) is usually associated with non-diffuse photon distributions and requires adjustments with respect to common diffusion model based studies, either in measurement

geometry [14] and/or method of analysis [14,15]. In this study, the diffusion model of Farrel *et al* was modified to a semi-empirical model by correcting for the initial underestimation of the measured $\mu_s'_{2nd}$ (Figure 3.2a). This correction contributes to the validity of our analysis, as shown in our phantom study. We speculate that the initial underestimation of $\mu_s'_{2nd}$ may be caused by the back reflection of photons into the medium at the aluminum probe surface, which is not accounted for in the boundary conditions of the diffusion model [10]. This may result in a more diffuse photon distribution for the relatively short source-detector separations in our setup. Fortunately, the underestimation is consistent and does therefore not affect our determination of μ_s', since the measured μ_s' agrees very well with the expected value for both Intralipid (Figure 3.2c) and polystyrene spheres after correction.

3.5.2 Model validity - patients

By using the diffusion model to analyze the optical properties of neonatal skin from the patient measurements, we implicitly assume that the probed volume consists of skin only, and is semi-infinite and homogeneous. It is known from literature that (preterm) neonatal skin exhibits no to little distinct variations between individual skin layers [16] and is therefore expected to be optically more homogeneous than adult human skin [17]. This difference in homogeneity between neonatal and adult skin is clearly reflected in the OCT images of Figure 3.9 a and b. The thickness of neonatal skin is not well reported in literature, but is expected to range between 0.65 and 1.5 mm [16,18]. Since the transition of the dermis into the subcutaneous tissue could not be observed in any of the OCT images of neonatal skin, we conclude that either no optical contrast exists between the dermis and the subcutaneous tissue (i.e. the optical coefficients are similar), or the skin thickness is larger than the imaging depth of the OCT system (approximately 1 mm). Therefore, we conclude that we measure the optical properties of skin only, since the probing depth of our system was assessed to be ~1 mm for a phantom comparable to neonatal skin (Section 3.3.2). Based on similar OCT images for other locations and patients (Section 3.4.3), we expect that our assumptions on homogeneity and semi-infinity are justified for all reported patient measurements. To further verify these assumptions, the optical properties would need to be measured at different depths in the tissue, which requires a small measurement volume from which the exact location inside the skin can be controlled. A potentially suited technique for this purpose is low-coherence spectroscopy (LCS) [19,20], although its performance *in vivo* has not yet been tested. LCS has the additional possibility of measuring the non-reduced scattering coefficient μ_s, instead of the reduced scattering coefficient μ_s' that is influenced by the scattering anisotropy **g** of the skin ($\mu_s' = \mu_s(1-\mathbf{g})$) [20].

3.5.3 Optical properties of neonatal skin

The optical properties of the skin of 60 patients were measured at the forehead, sternum, hand and foot. Comparison of the optical properties between the four measurement locations resulted in no significant differences. The spread of the optical properties is narrow for every location (Figure 3.5), ranging maximally 1.5 mm^{-1} between the 5^{th} and 95^{th} percentile of all measurements. However, this spread may be skewed, since the selection of patient measurements based on the validity limits results

in a reduction of measurements (Table 3.1). As a consequence, the lowest μ_s' values and the highest μ_a values are neglected in our presentation of the optical properties of neonatal skin (Figures 3.5 and 3.6). Figure 3.7 shows that the presented median values for μ_a of patients with skin type 3 should therefore be interpreted with caution, because μ_a changes considerably if the validity limits are neglected. Again, we would like to emphasize that the optical properties outside the validity limits should receive qualitative, rather than quantitative interpretation. For patients with skin type 1 and 2, very little measurements are lost and the presented values of μ_a can be trusted.

In line with the results of Saidi [4], the measured absorption coefficient spectra seem to contain mainly the contribution of oxygenized and deoxygenized hemoglobin, bilirubin and melanin. Laboratory analysis of sampled blood for a selection of patients yielded total hemoglobin levels in the range of 5 to 13 mmol/L and total serum bilirubin levels in the range of 40 to 400 µmol/L. The concentration of hemoglobin and bilirubin in the investigated tissue volume is affected by vessel density and bilirubin extravasation, and is therefore expected to be lower than in whole blood. The magnitude of the measured μ_a agrees well with the results of Saidi, who reported a range of approximately 0.2 to 1.3 mm^{-1} between 450 and 600 nm. More differences are found when comparing the measured values of μ_s' between this study and Saidi *et al* [4,5]. The reported average values of μ_s' by Saidi between 450 and 600 nm are considerably higher (~2-4 mm^{-1} [4]) than the median values of μ_s' presented in this study (Figure 3.5) and the spread of the data of Saidi is larger (standard deviation of ~3.6 mm^{-1} at 450 nm). Another remarkable difference exists in the dependency of μ_s' on gestational maturity. Whereas we found no to weak correlation between μ_s' and gestational maturity (Figure 3.6a), Saidi *et al* found much stronger correlation, which they ascribed to an increase of collagen fiber density in the skin during maturation [5]. Although small differences exist between the investigated patient populations and skin areas (abdomen in the study of Saidi) and not all of these results were published in peer reviewed journals [4], it is most likely that the observed differences in μ_s' are caused by unavoidable sample preparation procedures [6] for the *in vitro* tissue study of Saidi. However, it is expected that μ_s' will increase at a certain age outside the investigated age range in this study, since μ_s' is considerably higher for adult skin (3 – 9 mm^{-1}, measured *in vitro* between 450 – 600 nm) [21].

The measured values of μ_a for neonatal skin are comparable to adult skin (0.2 – 1 mm^{-1} between 450 – 600 nm) [21]. The absorption coefficient at 600 nm did not depend on gestational maturity, but did depend on postnatal age for patients with skin type 2 and 3 (Figure 3.8). This can be ascribed to the stimulated production of melanin after birth [12]. It is not expected that the suggested linear relation in Figure 3.8 will hold for all ages, because the increase of μ_a will level off at a certain age, which is approximately six months for neonates with a dark skin type [12]. Since melanin is located in the epidermal layer of the skin, the skin will be an optically layered medium for pigmented skin areas in neonates with high postnatal age. The homogeneity shown in the OCT scans of Figure 3.9 will therefore be lost. The reader should keep this in mind when using the presented optical properties, as well as the underestimation of μ_a for patients with a dark skin type. An increase of absorption due to tanning of the skin has also been described for neonates (gestational age ≥35.5 weeks) with skin type 1, receiving photo therapy [22]. Although the majority of our patient population with skin type 1 received

photo therapy during the measurement period, no increase of μ_a at 600 nm was observed for these patients (Figure 3.6b).

3.6 Conclusion

We measured *in vivo* the absorption and reduced scattering coefficients of neonatal skin for a large group of patients with varying gestational age, postnatal age and skin pigmentation. The optical properties did not differ significantly between different locations on the body (forehead, sternum, hand and foot). No to very weak correlation was observed between the optical properties and gestational maturity, but a strong dependency of the absorption coefficient on postnatal age existed for patients with skin type 3 (Negroid), which can be ascribed to the production of melanin after birth.

Knowledge of the optical properties of neonatal skin is invaluable when developing new, or improving existing optical diagnostic and therapeutic procedures that are used at the neonatal intensive care. We therefore hope that the results presented in this Chapter can contribute to the future development and improvement of these techniques.

References

1. K. Grohmann, M. Roser, B. Rolinski, I. Kadow, C. Müller, A. Goerlach-Graw, M. Nauck, H. Küster, "Bilirubin measurement for neonates: comparison of 9 frequently used methods", *Peadiatrics* **117**, 1174-1183 (2006)
2. J.W. Salyer, "Neonatal and pediatric pulse oximetry", *Respiratrory Care* **48**, 386-398 (2003)
3. M. Kaplan, V. Gold, C. Hammerman, A. Hochman, D. Goldschmidt, H.J. Vreman, D.K. Stevenson, "Phototherapy and photo-oxidation in premature neonates", *Biology of the Neonate* **87**, 44-50 (2005)
4. I.S. Saidi, "Optical properties of neonatal skin", Chap. 2 in Master Thesis*: Light transport in neonatal skin*, Rice University, Houston, TX (1990)
5. I.S. Saidi, S.L. Jacques, F.K. Tittel, "Mie and Rayleigh modeling of visible-light scattering in neonatal skin", *Appl. Opt.* **34**, 7410-7418 (1995)
6. R. Graaff, A.C. M. Dassel, M.H. Koelink, F.F.M. de Mul, J.G. Aarnoudse, W.G. Zijlstra, "Optical properties of human dermis in vitro and in vivo", *Appl. Opt.* **32**, 435-447 (1993)
7. R.M.P. Doornbos, R. Lang, M.C. Aalders, F.W. Cross, H.J.C.M. Sterenborg, "The determination of in vivo human tissue optical properties and absolute chromophore concentrations using spatially resolved steady-state diffuse reflectance spectroscopy", *Physics in Medicine and Biology* **44**, 967-981 (1999)
8. M.G. Nichols, E.L. Hull, T.H. Foster, "Design and testing of a white-light, steady state diffuse reflectance spectrometer for determination of optical properties of highly scattering systems", *Appl. Opt.* **36**, 93-104 (1997)
9. D. Arifler, C. MacAulay, M. Follen, R. Richards-Kortum, "Spatially resolved reflectance spectroscopy for diagnosis of cervical precancer: Monte Carlo modeling and comparison to clinical measurements", *Journal of Biomedical Optics* **11**, 064027 (2006)
10. T.J. Farrell, M.S. Patterson, B. Wilson, "A diffusion theory model of spatially resolved, steady-state diffuse reflectance for the noninvasive determination of tissue optical properties", *Med. Phys.* **19**, 879-888 (1992)
11. H.J. van Staveren, C.J.M. Moes, J. van Marle, S.A. Prahl, M.J.C. van Gemert, "Light scattering in Intralipid-10% in the wavelength range of 400-1100 nm", *Appl. Opt.* **30**, 4507-4514 (1991)
12. R.J. Walsh, "Variation in the melanin content of the skin of New Guinea natives at different ages", *Journal of Investigative Dermatology* **42**, 261-265 (1964)

13. A. Kim, R. Mathieu, F. Dadani, B.C. Wilson, "A fiberoptic reflectance probe with multiple source-collector separations to increase the dynamic range of derived tissue optical absorption and scattering coefficients", *Optics Express* **18**, 5580-5594 (2010)
14. S. Tseng, C. Hayakawa, J. Spanier, A.J. Durkin, "Investigation of a probe design for facilitating the uses of the standard photon diffusion equation at short source-detector separations: Monte Carlo simulations", *Journal of Biomedical Optics* **14**, 054043 (2009)
15. N. Rajaram, R.H. Nguyen, J.W. Tunnell, "Lookup table-based inverse model for determining optical properties of turbid media", *Journal of Biomedical Optics Letters* **13**, 050501 (2008)
16. Y.B. Chiou, U. Blume-Peytavi, "Stratum corneum maturation – a review of neonatal skin function", *Skin Pharmacology and Physiology* **17**, 57-66 (2004)
17. J. Welzel, "Optical coherence tomography in dermatology: a review", *Skin Research and Technology* **7**, 1-9 (2001)
18. P.H. Hoeger, "Physiology of neonatal skin", Chap. 2 in *Textbook of pediatric dermatology*, J. Harper, A. Oranje, N. Prose, Eds., pp. 42-47, Blackwell Publishing, Oxford, UK (2006)
19. N. Bosschaart, M.C.G. Aalders, D.J. Faber, J.J.A. Weda, M.J.C. van Gemert, T.G. van Leeuwen, "Quantitative measurements of absorption spectra in scattering media by low-coherence spectroscopy", *Optics Letters* **34**, 3746-3748 (2009)
20. N. Bosschaart, D.J. Faber, T.G. van Leeuwen, M.C.G. Aalders, "Measurements of wavelength dependent scattering and backscattering coefficients by low-coherence spectroscopy", *Journal of Biomedical Optics Letters* **16**, 030503 (2011)
21. E. Salomatina, B. Jiang, J. Novak, A.N. Yaroslavsky, "Optical properties of normal and cancerous human skin in the visible and near-infrared spectral range", *Journal of Biomedical Optics* **11**, 064026 (2006)
22. L.L. Randeberg, E.B. Roll, L.T.N. Nilsen, T. Chrystensen, L.O. Svaasand, "*In vivo* spectroscopy of jaundiced newborn skin reveals more than a bilirubin index", *Acta Peadiatrica* **94**, 65-71 (2005)